Rev.Adv.Mater.Sci. 15(2007) 158-166

STRUCTURAL AND OPTICAL STUDIES OF $NaNbO_3$ THIN FILMS GROWN BY PLD ON $SrRuO_3$ BOTTOM ELECTRODE

I. Aulika[1], J. Petzelt[2], J. Pokorny[2], A. Deyneka[2], V. Zauls[1] and K. Kundzins[1]

[1]Institute of Solid State Physics, University of Latvia 8 Kengaraga, Riga LV-1063, Latvia
[2]Institute of Physics, Academy of Science, Na Slovance 2, 182 21 Prague 8, Czech Republic

Received: January 22, 2007

Abstract. Sodium niobate $NaNbO_3$ thin films were deposited by the pulsed laser ablation (PLD) technique on $Si/SiO_2/Ti/Pt/SrRuO_3$ and $Si/SrRuO_3$ substrates. The structural and optical investigations were performed by X-Ray, micro Raman, ellipsometry and atomic force microscopy (AFM). The Raman spectra of NN have been studied at temperatures from 80 up to 743K at frequencies 200 - 1100 cm^{-1}. Optical properties were studied at photon energies 1.23 - 4.85 eV. Some Raman modes show lower frequencies, and the refractive index is higher for the NN films with smaller grains. The observed difference is discussed in terms of possible size induced phase transformation and/or grain boundary effects.

1. INTRODUCTION

Sodium niobate $NaNbO_3$ (NN) has attracted much attention and interest due to its high complexity and as promising lead-free piezoelectric material, environmentally more friendlier than, for example, PZT, and intriguing system due to the presence of six phase transitions (at 173, 638, 753, 793, 845, and 913K) in the temperature range 20 - 1000K changing its phase from high-temperature paraelectric (PE) to antiferrodistortive and then antiferroelectric (AFE) phase at 638K [1,2]. The physical properties such as electrical or optical properties, crystalline structure, *etc*. of NN powders [3,4], single crystals [5-9], and ceramics [9-13] have been widely studied within the last 55 years, while just few studies of the dielectric properties, Raman spectroscopy, and X-ray diffraction of NN thin films on $SrRuO_3(100)/SrTiO_3(100)$ [12] and Si [14] have been recently reported.

No work has been published concerning a comparison of highly crystalline NN thin films with $SrRuO_3$ (SRO) coated $Si/SiO_2/Ti/Pt/$ and Si substrates deposited by PLD. For our best knowledge, there are no publications yet of complex refractive index dispersion of NN thin films, too. The structure and optical studies are important of NN films because of its possible applications in optoelectronic devices based on optical waveguides, which require well-crystallized thin films with high transparency in order to minimize the transmission loss. The structural and optical properties such as x-ray, Raman scattering, surface morphology and dispersion of the complex refractive index of the NN heterostructures are investigated and discussed in this work.

Corresponding author: I. Aulika, e-mail: aulika@lanet.lv

2. EXPERIMENTAL

Sodium niobate $NaNbO_3$ thin film heterostructures were deposited by PLD on Si((100), 300 μm)/SiO_2(1000 nm)/Ti(7 nm)/Pt((111), 50 nm)/$SrRuO_3$ (~ 30 nm) and Si/$SrRuO_3$ substrates using KrF-excimer laser (LPX 300, Lambda Physics) with the wavelength of 248 nm, and the repetition rate of 10 s^{-1} with energy density of 2 - 3 J/cm^{-2}. PLD process was accomplished in the vacuum chamber with Ar/O_2 atmosphere. The laser beam was focused on the target material, which was wobbling and rotating in order to minimize the droplet formation. The deposition temperature (T_d) for NN and SRO was T_d = 850K. The thin Ti layers were grown by a thermal evaporation process at a temperature of 1170K. Platinum bottom and top electrodes were sputtered by the e-beam method, keeping the substrate temperature around 470K. The targets of the NN and SRO were made by chemical synthesis technique [15].

The highly conductive oxide $SrRuO_3$ have been used as the bottom electrode due to its stability, not only in oxidizing, but also in inert gas atmospheres up to quite high temperatures [16–18], unlike the high-T_c superconducting thin films, which typically have relatively poor crystalline quality and rough surfaces, and are not fully chemically and thermally stable. High stability of the bottom electrode and processing compatibility with ultra-large-scale integrated circuit fabrication during electrode deposition are very important to realize the integration between the high-permittivity dielectric materials and active devices located on the substrates.

The crystal structure of the films was analyzed using Siemens D5000 X-ray diffraction (XRD) equipment with Co anode. The dielectric properties of the films were investigated in a frequency range from 20 Hz to 250 kHz and at temperatures from 290K up to 620K at 10 mV by a probe station with a Perkin Elmer 7265 lock-in amplifier.

The optical measurements were performed by means of a J. A. Woollam spectroscopic ellipsometer operating in rotating analyzer mode. The main ellipsometric angles ψ and Δ were measured in a spectral range from 250 to 1000 nm (1.23 eV till 4.85 eV) at incidence angles of 65, 70 and 75 degrees. Two models were chosen to fit experimental data: 1) relatively simple model, where sample compose of the substrate, film and top layer of superficial roughness (a mixture of the void (air) and the underlying material), and 2) relatively more complex model with the same amount of layers

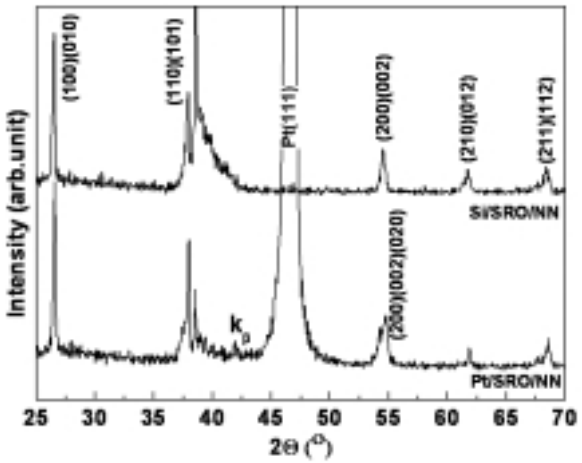

Fig. 1. X-ray diffraction studies using 2θ scans for NN thin films on 2 different substrates - Pt/SRO and Si/SRO.

like in the 1st case, but film was considered to be as a mixture of material and voids (grain boundary effect). The top layer and film as a mixture of material and grain boundaries was described in terms of the effective medium approximation (EMA) [19]:

$$\frac{\varepsilon_e - \varepsilon_h}{\varepsilon_e + y\varepsilon_h} = \sum_{i=1}^{n} f_i \frac{\varepsilon_i - \varepsilon_h}{\varepsilon_i + y\varepsilon_h},$$

where f_i and ε_i are the volume fractions and complex dielectric constant of material (component) i, ε_e and ε_h are the dielectric functions of the EMA (total system) and the host material, respectively. The quantity n is the number of components or materials, which are mixed together to form the EMA material. The screening parameter or depolarization factor [19], is related to the parameter $y = 1/m - 1$, where m – screening factor ($0 \le m \le 1$). Screening factor describes the microstructure of the mixtures: 1 corresponds to a flat disk, 1/3 – to a spherical microstructure, and screening factor 0 - to a columnar microstructure. The thickness of the top layer correlates with the root mean square (RMS) value of the surface roughness provided that the percentage of voids is set to 50% and the screening parameter is assumed to be 0.33. The value assigned to the host dielectric function depends on which EMA model is being used. The Maxwell-Garnett equation [19] was used to model film as EMA to provide that the 1st material is the host material (dielectric, for example) $\varepsilon_h = \varepsilon_1$. If the host material is void ($\varepsilon_h = 1$) as in the case of mod-

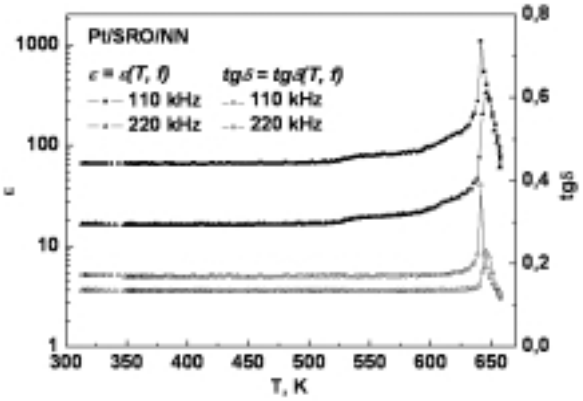

Fig. 2. Dielectric permittivity ε (solid symbols) and loss factor tgδ (open symbols) as the function of the temperature at frequencies of 110 kHz and 220 kHz.

elling the top layer of the film, the EMA equation reduces to the Lorentz-Lorenz model [19]:

$$\frac{\varepsilon_e - 1}{\varepsilon_e - y} = \sum_{i=1}^{n} f_i \frac{\varepsilon_i - 1}{\varepsilon_i - y}.$$

The Lorentz oscillator for the dielectric function was used to describe the optical properties of NN [19, 20]:

$$\varepsilon = \varepsilon_\infty \left(1 + \sum_{j=1}^{k} \frac{A_j^2}{(E_c)_j^2 - E(E - i\nu)} \right).$$

Model parameters k, ε_∞, E_c, E, u and A_j are respectively: number of oscillators, high-frequency lattice dielectric constant, the centre energy of each oscillator in eV, photon energy in eV, vibration damping (broadening) of the j-th oscillator in eV, and amplitude (strength) of each oscillator in eV. In our work a single Lorentz oscillator was used to describe the complex dielectric function. The optimal values for the refractive index n, extinction coefficient k, and thickness d for each sample layer were found by Monte-Carlo optimisation of the multilayer model. The minimum root mean squared error (RMSE) was used as a flag (condition) to terminate the optimization.

Raman spectroscopy was performed by a RENISHAW micro Raman spectrometer in a temperature range 80 - 743K and in a frequency range from 200-1100 cm^{-1}.

The surface morphology was examined using AFM. For AFM measurements a Stand Alone SMENA microscope (NT-MDT Co.) was employed[2] in a contact mode using conventional silicon tips (spring constant ~ 30 N/m, resonance frequency ~ 350 kHz). The deflection set point was 0.5, the s-point parameter of probe and surface interaction, maintained via feedback during the scanning, was zero amperes, with the integrator gain coefficient included in the general feedback loop coefficient being 1.5 nA. The scanned area was varied from (10×10) to (0.5×0.5) μm on the different pleases of the sample surface, with the scanning rate 0.8 – 1 Hz.

3. RESULTS

The XRD patterns show that NN has orthorhombic crystal structure (Fig. 1) on both substrates deposited at 850K, which corresponds to that reported for the single crystals [2]. The broadening of the peaks, which corresponds to (110) and (211) lattice planes, as well as broadening of the peak at ~ 40° conform to the diffraction pattern of Pt and SRO bottom electrodes.

Fig. 2 shows the dielectric permittivity ε and loss factor tgδ as a function of temperature (T) for Pt/SRO/NN, with appreciable frequency dependence of the dielectric permittivity ε(T) (110 kHz and 220 kHz); as the frequency increase, the value of ε_{max} decreases and T_c slightly shifts to the higher temperature - 646K. According to the sharp phase transition, chosen heating rate of 2 K/min was too high, so that certain degree of inaccuracy of about ±2K for the established T_c has to be considered. The anomalous peak in ε and tgδ at T_c corresponds to the one transition (P to R) from a series phase transitions of NN, which are [2]

$$N\left(R3c \,/\, C_{3v}^{6}\right) \xrightarrow{173K} P\left(Pbma \,/\, D_{2h}^{11}\right) \xrightarrow{638K}$$

$$R\left(Pmnm \,/\, D_{2h}^{13}\right) \xrightarrow{753K} S\left(Pnmm \,/\, D_{2h}^{13}\right) \xrightarrow{793K}$$

$$T1\left(Ccmm \,/\, D_{2h}^{17}\right) \xrightarrow{845K}$$

$$T2\left(P4 \,/\, mbm \,/\, D_{4h}^{5}\right) \xrightarrow{913K} C\left(Pm3m \,/\, O_h^1\right)$$

In these phases, N is trigonal, P, R, S and T1 are orthorhombic, T2 is tetragonal, and C is cubic. The same behaviour of ε(T) and tgδ(T) (a sharp increase of ε and tgδ) was observed for NN single crystals [8,9] and ceramics [12]. Detected T_c is in a good agreement with that of the single crystals [2,6,8,9] and ceramics [12,13]. ε and tgδ at 1 kHz at room

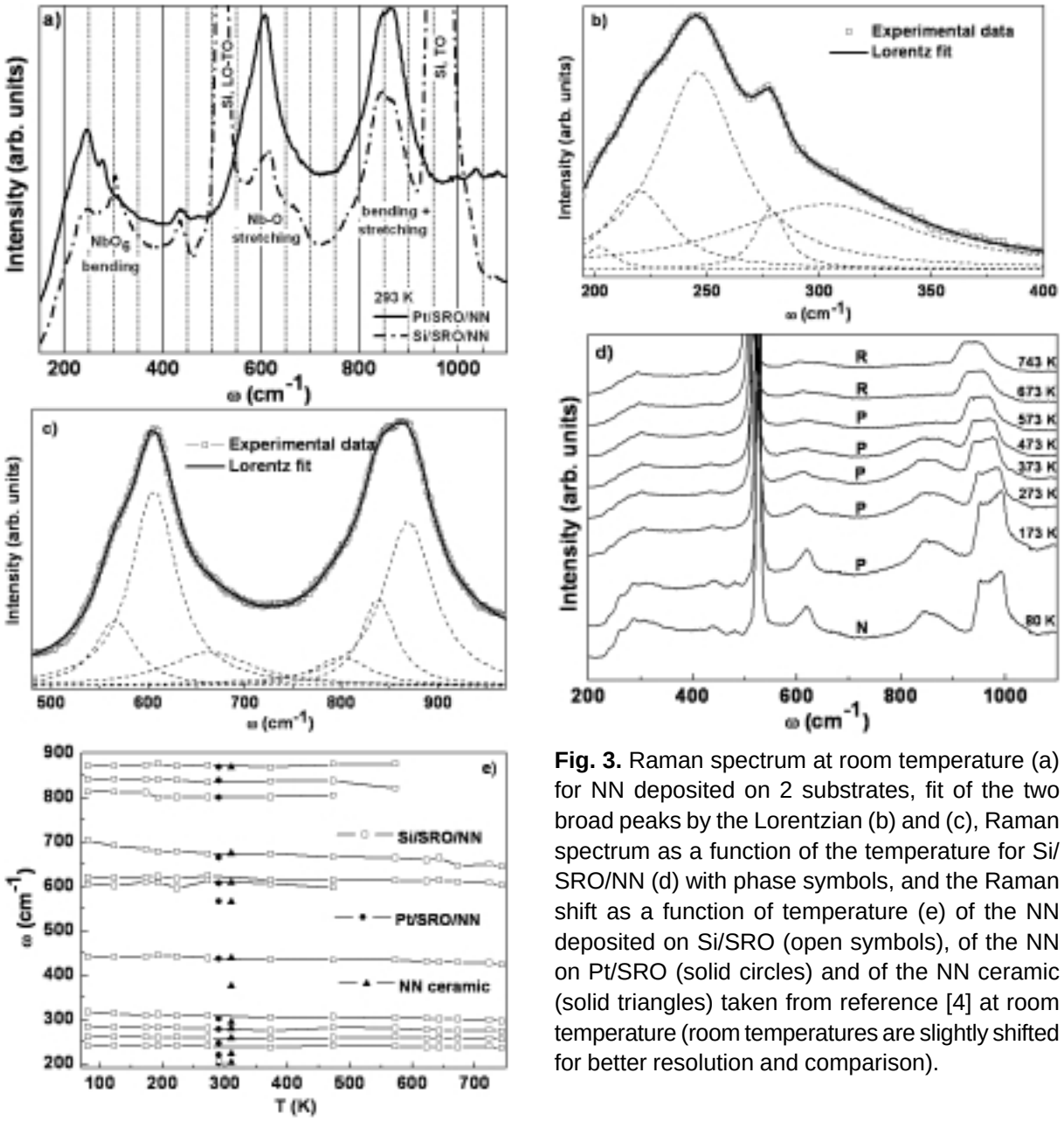

Fig. 3. Raman spectrum at room temperature (a) for NN deposited on 2 substrates, fit of the two broad peaks by the Lorentzian (b) and (c), Raman spectrum as a function of the temperature for Si/SRO/NN (d) with phase symbols, and the Raman shift as a function of temperature (e) of the NN deposited on Si/SRO (open symbols), of the NN on Pt/SRO (solid circles) and of the NN ceramic (solid triangles) taken from reference [4] at room temperature (room temperatures are slightly shifted for better resolution and comparison).

temperature is 200 and 0.3, respectively. Our ε is lower and tgδ is higher compared with established by Saito [12] (ε and tgδ are 252 and 0.03, respectively, for NN with a thickness of 780 nm deposited by PLD on SRO/$SrTiO_3$ substrate), and measured on single crystals [9] and ceramics [13], but in good agreement with detected dielectric values by Matthias [6] for less perfect NN crystals.

Fig. 3 shows the Raman spectra of NN samples at 200 – 1100 cm^{-1}, corrected by the Bose-Einstein temperature factor. The broad peaks at ~ 240, 620, and 850 cm^{-1} were deconvoluted successfully (Figs. 3b and 3c) and can be reproduced by superposition of 5, 3, and 3 Lorentzians, respectively. Such broad three bands were observed also for NN powders [14,21] and one broad band at ~ 600 cm^{-1} for ceramics [4].

At room temperature totally 12 Raman bands were observed in our experiments. The broad bands in the 620 cm^{-1} and 850 cm^{-1} region consist

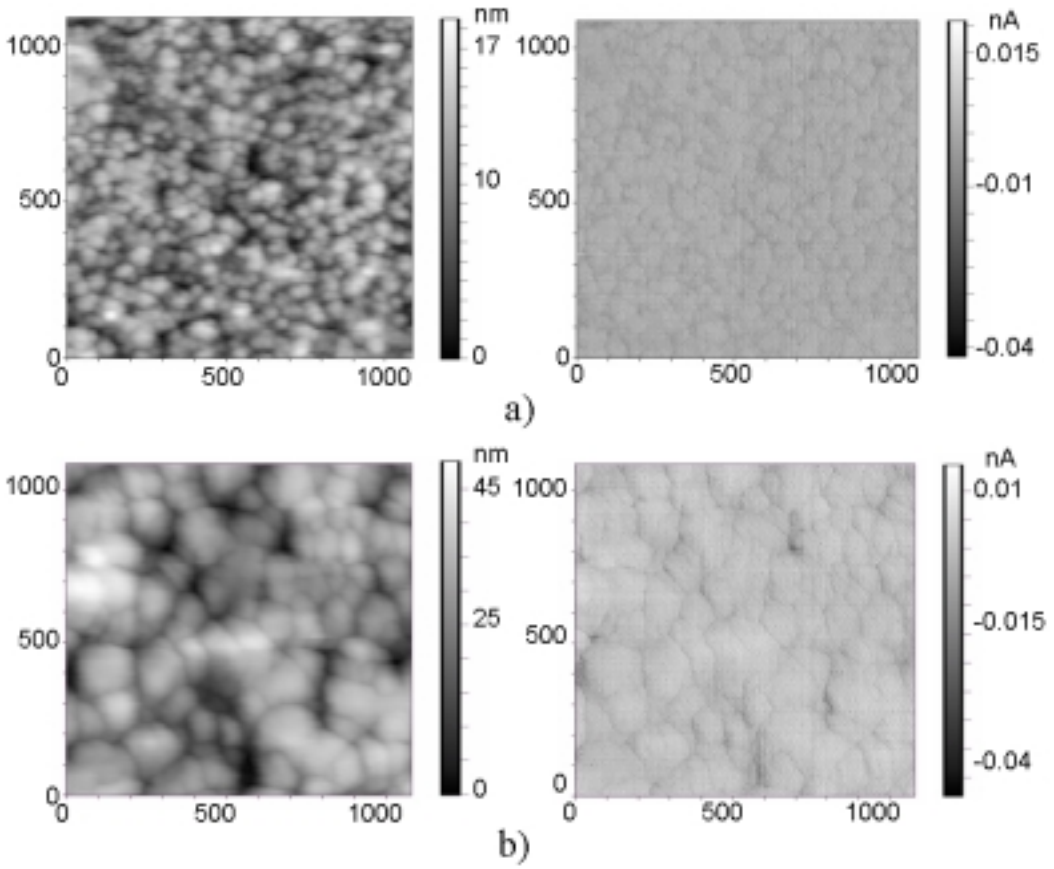

Fig. 4. Surface topography (left) and lateral force images (right) with scanned area (1×1) μm for NN on a) Pt/SRO, and b) Si/SRO. The RMS roughness for the given images is 3 and 8 nm.

of two strong peaks at 605 and 869 cm^{-1} with two shoulder bands for Pt/SRO/NN, and 615 and 835 cm^{-1} also with two shoulder bands for Si/SRO/NN (Fig. 3c). These peaks can be attributed to the internal modes of the Nb-O stretching and combination of stretching and bending [21,22]. The broad peak at ~ 240 cm^{-1}, in accordance with literature, is due to the NbO_6 interbond angle bending [22,23].

Raman spectra at various temperatures of NN on heating are shown in Fig. 3d. Almost all peaks can be resolved up to 743K: above 200K, the band at ~ 480 cm^{-1} with weak intensity vanishes, and above 573K the broad peak at ~ 835 cm^{-1} vanishes. All the Raman bands show the expected broadening with increasing temperature. Raman mode shifts ω as the function of the temperature for NN on SRO/Si are given in Fig. 3e. Up to 743K, the Raman spectra are not strongly temperature dependent except for the broad peaks at ~ 615 and 835 cm^{-1}. It can be seen that the second-order shoulder bands around 615 and 835 cm^{-1} can be detected only up to 473K. Similar results were found in the work of Wang [4]: there is one strong peak and two shoulder bands at ~ 600 cm^{-1}, which exist from room temperature up to 460 K, and above 460 K one shoulder band vanishes. The modes at ~ 240 and 620 cm^{-1} of NN deposited on Pt/SRO are shifted to lower values of ω in comparison with those of NN on Si/SRO and for NN ceramics [4] (Figs. 3 a, e). Only two modes at 437 and 673 cm^{-1} of the Pt/SRO/NN and Si/SRO/NN are comparable with the data of ceramics. The modes of Pt/SRO/NN at 568, 607, and 869 cm^{-1}, and of Si/SRO/NN at 259 and 280 cm^{-1} are the same as those of ceramics (Fig. 3c), but with slightly differeces between the films. The higher values of ω at 309, 612, 624, and 873 cm^{-1} for Si/SRO/NN and lower values ω at 219 and 247 cm^{-1} in comparison with ceramics can be due to the strain at the film/substrate interface, which appears due to the lattice mismatch of the

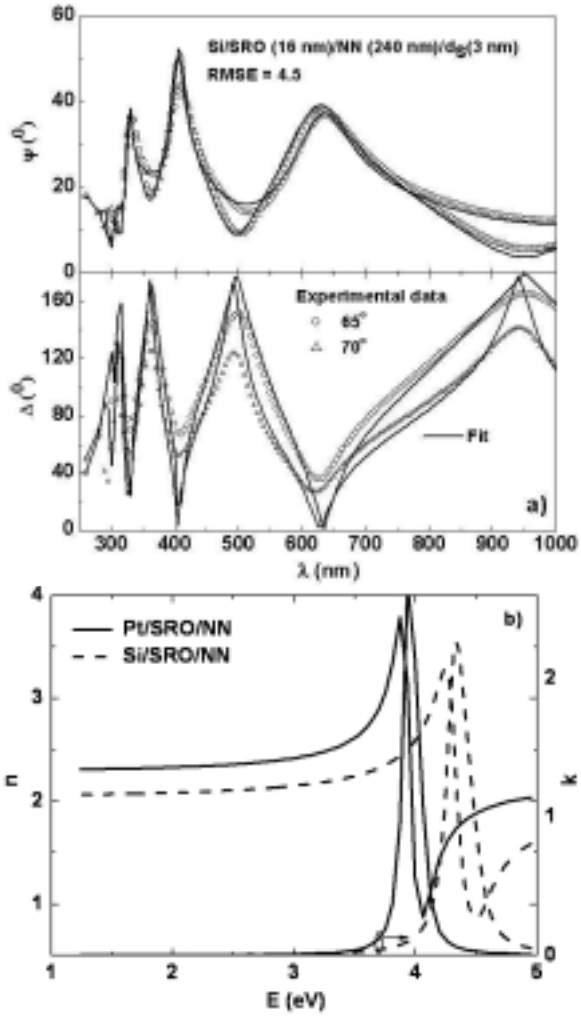

Fig. 5. Experimental main ellipsometric angles ψ and Δ (open symboles) and their numerical fit (solid line) as a function of wavelength at two incident angles for the Si/SRO/NN sample (a); refractive coefficient *n* (the left axis) and extinction coefficient *k* (the right axis) of NN films deposited on Pt/SRO (solid line) and Si/SRO (dashed line) substrates (b).

film and substrate. However, a size-induced phase transformation and/or grain boundary effects can also be an explanation of the established distinction, which will be discussed below.

Surface morphology images detected by AFM are given in Fig. 4. The surface of PLD NN films is very smooth: the mean value for all calculated root mean square (RMS) roughness of the films is 3 and 6 nm for NN on Pt/SRO and Si/SRO, respectively. The average grain size is around 50 and 100 nm for NN on Pt/SRO and Si/SRO, respectively. NN films were grown on two different substrates simultaneously, but the higher heat treatment temperature and the substrate and uniformity of the plasma beam may act as a nucleation centre and help the grains to grow larger on the Si/SRO substrate. The local friction force (lateral force) over the sample surface is given in Fig. 4. It can be seen that the angle of torsion is not changing, which means that the surface is uniform without different zones of different friction factors. The AFM morphology confirmed that a dense and smooth NN thin film can be deposited by PLD on Pt/SRO and Si/SRO substrates.

Fig. 5a illustrates an experimental data and the second model numerical fit of the main ellipsometric angles ψ and Δ as a function of the wavelength at the incidence angles 65° and 70° for Si/SRO/NN sample. The RMSE value for the first model was 9, but for the second one 4. The simple model, where the sample was considered to consist just from the substrate, film, and top layer, could not give such good agreement between measured spectra and calculated one as it was established assuming that the film is a mixture of the host material and the voids. Significant difference in the amplitude of the calculated Δ in comparison with the measured one, is due to the thickness non-uniformity of the film. The thickness distribution of the thin films rise depolarization of the light and it can be seen as the rounded shape of minima and maxima in Δ (since Δ is very sensitive to the thickness). The high-frequency lattice dielectric constant and volume fraction for the second phase of NN material was established to be 1.1 and 35%, respectively. The ε_∞ band gap energy for the 2nd phase is much lower then that for the host material of NN film (see Table. 1). Similar results were detected for Pt/SRO/NN sample, too.

Optical properties for NN deposited on the two substrates are shown in Fig. 5b. The refractive index *n* and the absorption index *k* increase as the energy increases from 1.17 to 3.86 eV for NN on Pt/SRO and to 4.24 eV for NN on Si/SRO (normal dispersion) and decrease at energy from 3.86 to 4.06 eV and from 4.24 to 4.49 eV (anomalous dispersion), respectively, which is usual for dielectric materials in that energy range. The *n* dispersion curve is lower for NN on Si/SRO, but the centre energy of the oscillator is at higher photon energies than for NN on Pt/SRO. The changes in the optical properties can be due to the strains induced

Table. 1. Physical parameters of NN films deposited on the two different substrates.

Substrate	d_{SRO} (nm)	d_{NN} (nm)	d_s (nm)	S_q (nm)	n_{633}	E_g (eV)	ε_∞	E_c (eV)	υ (eV)	A (eV)
Pt/SRO	20	160	2	3	2.33	3.35	4.86	3.91	0.06	1.09
Si/SRO	16	240	4	6	2.08	3.48	3.79	4.31	0.16	1.44

by the substrate, which modifies the electronic structure and leads to the difference in n and E_g.

The fundamental absorption edge for each film was deduced from the spectral dependence of the imaginary part of dielectric constant $\varepsilon_2 = 2nk$ by applying the Tauc relation [24,25] $\hbar\omega\varepsilon_2 = \text{const}\cdot(\hbar\omega - E_g)^l$, where $\hbar$ is reduced Planck constant, ω - angular frequency, E_g – band gap energy, and $l = 1/2$ for the allowed direct transitions and 2 for indirect transitions. By extrapolating the linear part [26], the optical energy gap was deduced at $\varepsilon_2(h\nu)^{1/2} = 0$, giving the fundamental absorption age E_g for the direct transition (see Table 1).

The thickness d_{SRO} of the SRO, d_{NN} of NN thin films, and surface layer d_s, (RMS) roughness S_q detected by AFM, refractive index n_{633} at 633 nm, and fitting parameters of the single Lorentz oscillator: optical band gap energy E_g, high-frequency lattice dielectric constant ε_∞, centre energy of the oscillator E_c, vibrational broadening of the oscillator u and amplitude (strength) of the oscillator A, are summarized in Table 1. The refractive coefficient is lower for NN deposited on Si/SRO, but E_g is higher than that for the NN on Pt/SRO. Detected n for Pt/SRO/NN sample is in good agreement with values detected for single crystals [2]. The RMS surface roughness obtained by the model fitting is consistent with that measured by AFM.

4. DISCUSSION

In our work the Raman shift frequencies and optical properties of Pt/SRO/NN film with smaller grains and lower roughness was established to be different from those detected for Si/SRO/NN film with bigger grains and higher value of the roughness. This can be caused by the fact that the Pt/SRO/NN film is denser and less stressed at the film/substrate interface that the Si/SRO/NN film. But it could be also due to the size-induced phase transformation of the NN: some specific bands are drastically shifted to the lower wavenumber region on decreasing the grain size. One of the most recent explanations is based on increase in the internal pressure due to the surface curvature and small particle radius (Gibbs-Thomson effect) [27]. It is one of the possible mechanisms for stabilization of more symmetric structures than the transformation from the thermodynamically stable ones at ambient temperature and pressure - transition from a more symmetric to a less symmetric structure attended with a decrement of the lattice. In the work of Shiratori a size-induced phase transformation from a monoclinic structure to a triclinic structure was discovered for $(K_{0.50},Na_{0.50})NbO_3$ (KNN) powders at a critical size of about 200 nm [27]. The perovskite cell volume of KNN increased due to the transformation, induced by decreasing particle size. Result of KNN is opposite to that for NN powders [21] and makes us to believe that ionic distributions (K/Na) or charge distribution processes resulted in volume expansion [29] as a driving force of this phase transformation. If the grains are small, it is more complicated to implement homogeneous ionic distribution than when the grains are large. In the case of NN, there is no difficulty of such distribution and therefore Gibbs-Thomson effect is likely to be the responsible transformation mechanism. Insomuch as the size induced phase transformation was detected for the powder and not for the thin films, and in our work the difference in the grain size is much smaller then that for Shiratori samples, to be sure weather this kind of effect can be consistent for NN thin films, we need to provide series of additional measurements with samples of the wide range of grain sizes.

Another substantial explanation of detected deference in the optical and Raman spectra could be the grain boundary effects. From the modelling of ellipsometric measurements, it was established that it was not possible to improve experimental results by using only surface roughness layer even for the high values of d_s > 20 nm. When the film was assumed to be as a mixture of 2 materials, the fit significantly improved.

If the sample is inhomogeneous, then its effective dielectric response usually can be determined, which does not give full information about the spatial variation of the dielectric function. The inhomogeneous material often can be considered as a densely filled micro-composite formed by individual, dielectrically homogeneous parts. Depolarization field, which always appears on the boundaries between the different parts, tends to reduce the probing electric field in the higher-permittivity parts. As the result, there can be pronounced differences between the effective dielectric response and the response of individual homogeneous parts.

The EMA model is particularly useful in describing the properties of inhomogeneous, granular materials (ceramics, polycrystalline films), in which the grain boundary region (shell) plays the role of the second component whose dielectric properties may differ from that of the bulk (core) [30,31]. In high-permittivity materials this region has usually lower permittivity (in ferroelectrics it might be non-ferroelectric - dead or passive layer) and in semiconductive ceramics it may differ in conductivity (e. g. blocking boundaries in grain-boundary capacitors). From fitting the 2nd model to the ellipsometric data, the smaller value of high-frequency lattice dielectric constant, and smaller values of optical constants and band gap energy was found. The evidence of the lower permittivity parts in the sample can be found also from dielectric results of NN films: it was detected that dielectric permittivity is lower and dielectric losses are higher then those for bulk materials, but in good agreement with the results of less crystalline samples. Such difference can be due to the defects localized on the grains and/or grain boundaries.

Properties of phonon modes, specially the soft modes, in thin films should obviously reflect the substrate-induced stresses, but in addition to that, influence of grain boundary effects and interfacial layers between the film and substrate or electrode can be very important or even dominant [32]. According to our results on optical and dielectric properties we believe that detected difference between Raman shift frequencies of the films and bulk materials can be caused not only from size impacts, but also from the grain boundary effects.

5. CONCLUSION

$NaNbO_3$ thin films with a flat surface morphology and good crystallinity were deposited on substrates of Pt/SRO and Si/SRO. The structural and optical properties of the films were analyzed using X-ray diffraction analysis, Raman spectroscopy, AFM, and spectroscopic ellipsometry.

Almost all expected phonon modes were detected simultaneously in the Raman spectra due to the random distribution of the crystallographic axes in the granular samples for NN films. The Raman mode shifts ω at ~ 240 and 620 cm^{-1} of NN deposited on Pt/SRO lay at lower values of ω in comparison with those of NN on Si/SRO.

Detected reduced value of the dielectric permittivity and enlarged value of the loss factor for Pt/SRO/NN film, shift in phonon modes frequencies for NN thin films in comparison with ceramics as well as lower refractive index of the second phase might be due to the size-induced phase transformation and/or grain boundary effects.

Applying a multilayer model, where the film was considered to consist from host material and voids (grain boundary effect), to the experimental data, the good numerical fit to experimental data was found. Refractive index of Pt/SRO/NN samples is in a good agreement with that detected for single crystals.

ACNOWLEDGEMENTS

This research was supported by the COST fellowship, European Social Fund and K. Morberg scholarship of the University of Latvia. The author wants to thank the Solid States and Material Research in Dresden (Germany), Atomic Institute in Vienna (Austria), and Institute of Physics, Academy of Science in Prague (Czech Republic) for co-operation in the PLD technique, dielectric, Raman spectroscopy and ellipsometry measurements were performed.

REFERENCE

[1] H. D. Megaw // *Ferroelectrics* **7** (1974) 87.
[2] NAME Landold-Bornstein, *Ferroelectric and Related Substances* **16** (1981) 45.
[3] M. H. Lentea, J. de Los S. Guerraa, J.A. Eirasa and S. Lanfredi // *Sol. St. Com.* **131** (2004) 279.
[4] X. B. Wang, Z.X. Shen, Z.P. Hu, L. Qin, S.H. Tang and M.H. Kuok // *J. Mol. Str.* **385** (1996) 1.
[5] A. Molak // *Sol. St. Commun.* **62** (1987) 413.
[6] B. T. Matthias and J. P. Remeika // *Phys. Rev.* **82** (1951) 727.
[7] M. Drulis and K. Konieczny // *Mat. Sc. Eng.* **B72** (2000) 19.

[8] K. Konieczny // *Mat. Sc. Eng.* **B60** (1999) 124.
[9] G. Shirane, R. Newnham and R. Pepinsky // *Phys. Rev.* **96**, 3 (1954) 581.
[10] S. Lanfredi, L. Dessemond and A.C. Martins Rodrigues // *J. Europ. Cer. Soc.* **20** (2000) 983.
[11] L. Pardo and P. Duran-Martin // *J. Phys. Chem Solids* **58** (1997) 1335.
[12] T. Saito, H. Adachi, T. Wada and H. Adachi // *Jpn. J. Appl. Phys.* **44** (2005) 6969.
[13] L. A. Reznitchenko and A. V. Turik // *J. Phys.: Condens. Matter* **13** (2001) 3875.
[14] Zhenxiang Cheng, Kiyoshi Ozawa and Minoru Osada // *J. Amer. Cer. Soc.* **89** (2006) 1188.
[15] M. Dambekalne, M. Antonova and M. Livinsh // *J. Europ. Cer. Soc.* **26** (2006) 2963.
[16] Q. Gan, R.A. Rao, C.B. Eom, J.L. Garrett and M. Lee // *Appl. Phys. Lett.* **72** (1998) 978.
[17] C. B. Eom, R. B. V. Dover, J. M. Phillips and D.J. Werder // *Appl. Phys. Lett.* **63** (1993) 2570.
[18] Q. X. Jia, X.D. Wu, S.R. Foltyn and P. Tiwari // *Appl. Phys. Lett.* **66** (1995) 2197.
[19] S. Bosch, J. Ferre-Borrull and N. Sancho-Parraamon // *J. Sol. St. Elec.* **45** (2001) 703.
[20] D.E. Aspnes, J.B. Theeten and F. Hottier // *Phys. Rev. B* **20** (1979) 3292.
[21] Y. Shiratori and A. Magrez // *J. Phys. Chem. B* **109** (2005) 20122.
[22] Yu. I. Yuzyuk, P. Simon and E. Gagarina // *J. Phys.: Condens. Matter* **17** (2005) 4977.
[23] E. Bouziane, M. D. Fontana and M. Ayadi // *J. Phys.: Condens. Matter* **15** (2003) 1387.
[24] J.C. Tauc, *Optical Properties of Solids* (North-Holland, Amsterdam, 1972).
[25] E.A. Davis and N.F. Mott // *Phil. Mag.* **22** (1970) 903.
[26] I. Aulika, V. Zauls, K. Kundzins, M. Kundzins and S. Katholt // *J. Optoel. Adv. Mat.* **5** (2003) 755.
[27] T. Chraska, A. H. King and C. C. Berndt // *Mater. Sci. Eng.* **A28**6 (2000) 169.
[28] Y. Shiratori, A. Magrez and C. Pithan // *Chem. Phys. Lett.* **391** (2004) 288.
[29] M. Ya. Gamarnik // *Phys. Stat. Sol.* (b) **164** (1991) 107.
[30] D.J. Bergman and D. Stroud, In: *Sol. State Phys. 46*, ed. by H. Ehrenreich and D. Turnbull (Academic Press, Boston, 1992) p. 147.
[31] D.A.G. Bruggeman // Ann. Phys. (Berlin) **24** (1935) 636.
[32] J. Petzelt, T. Ostapchuk and R. Gregora // *Phys. Rev. B.*, submitted.